Electroosmotic Flow Control in Complex Microgeometries

Prashanta Dutta, Ali Beskok, and Timothy C. Warburton

***Abstract*—Numerical simulation results for pure electroosmotic and combined electroosmotic/pressure driven Stokes flows are presented in the cross-flow and Y-split junctions. The numerical algorithm is based on a mixed structured/unstructured spectral element formulation, which results in high-order accurate resolution of thin electric double layers with discretization flexibility for complex engineering geometries. The results for pure electroosmotic flows in cross-flow junctions under multiple electric fields show similarities between the electric and velocity fields. The combined electroosmotic/pressure driven flows are also simulated by regulating the flowrate in different branches of the cross-flow junctions. Flow control in the Stokes flow regime is shown to have linear dependence on the magnitude of the externally applied electric field, both for pure electroosmotic and combined flows. This linear behavior enables utilization of electroosmotic forces as nonmechanical means of flow control for microfluidic applications. [616]**

***Index Terms*—Electroosmotic flow, flow control, h/p element method, microfluidics, spectral element method.**

I. Introduction

DEVELOPMENTS in microfabrication technologies have recently enabled a variety of miniaturized fluidic systems consisting of microducts, valves, pumps and mixers, which can be utilized for medical, pharmaceutical, defense and environmental monitoring applications. Examples of such applications are drug delivery, DNA analysis/sequencing systems and biological/chemical agent detection sensors on microchips. These microfluidic systems require seamless integration of sample collection, separation, biological and chemical detection units with fluid pumping, flow control elements and the necessary electronics on a single microchip. The reliability and compliance of these components are important for successful design and operation of the entire microfluidic system. Especially, the subsystems like microvalves and micropumps with moving components are complicated to design and fabricate, and they are prone to mechanical failure due to fatigue and fabrication defects. In this paper, we explore new ideas of *microflow control elements* using the electrokinetic flow control schemes with nonmoving components.

The electrokinetic effects were discovered by Reuss in 1809 [1]. Since then, there has been many theoretical and experimental studies. The most influential contribution is the development of the electric double layer theory by Helmholtz (1879), which related the electrical and flow parameters for electrokinetic transport. Based on this theory, the mixed electroosmotic/pressure driven flows are analyzed for very thin two-dimensional slits [2]–[4], and thin cylindrical capillaries [5].

Experimental measurements of electrokinetically driven micro-flows are obtained by the molecular fluorescence tagging (MFT) and microparticle image velocimetry techniques (μ-PIV). Based on these, the velocity vector field in the mixed electrokinetic/pressure driven microchannel flows are measured [6]; dependence of the fluid velocity and the dispersion rate on the surface electric charge distribution are studied [7]; and efficient flow control mechanisms in micro-channels are demonstrated [8].

There has been a growing interest on numerical simulation of electrokinetically driven microflows. Recently, micro-injection through intersection of two-channels has been studied using a finite volume formulation based on the Debye–Hückel linearization [9]. Electroosmotic and electrophoretic transport and species diffusion have been studied by a finite difference algorithm for two-dimensional complex geometry flow conduits [10]. Electroosmotically driven micro-flows in T-junctions are studied by a finite element formulation [11] and also by using meshless finite cloud algorithms [12]. Liquid flow and forced convection heat transfer in electroosmotically driven micro-channels are also analyzed using a finite difference method [13], [14].

Motivated by development of microfluidic flow control elements with nonmoving components, we numerically explore electroosmotic flow control schemes in various micro-channel configurations. The numerical algorithm is based on an unstructured spectral element method, which delivers flexibility of complex geometry discretization with high-order accuracy. This paper is organized as follows: In Section II, the electric double layer concept is introduced. In Section III, the governing equations for the electroosmotically driven flows are presented. The numerical algorithm and numerical accuracy issues are addressed. In Section IV, electroosmotic flow control concepts in cross-flow junction and Y-junction geometries are demonstrated. Finally, in Section V conclusions of our work are presented.

II. Electric Double Layer (EDL)

The electric double layer (EDL) is formed due to the presence of static charges on the surfaces. Generally a dielectric surface acquires charges when it is in contact with a polar medium, by chemical reaction, ionization or ion absorption. For example,

Manuscript received August 18, 2000; revised July 13, 2001. This work was supported by the Texas Higher Education Council Advanced Research Program (000512-0418-1999). Subject Editor T. Kenny.

P. Dutta is with the School of Mechanical and Materials Engineering, Washington State University, Pullman, WA 99164-2920 USA.

A. Beskok is with the Mechanical Engineering Department, Texas A&M University, College Station, TX 77843-3123 USA (e-mail: abeskok@mengr.tamu.edu).

T. C. Warburton is with the Department of Mathematics and Statistics, University of New Mexico, Albuquerque, NM 87131-1141 USA.

Publisher Item Identifier S 1057-7157(02)00504-8.

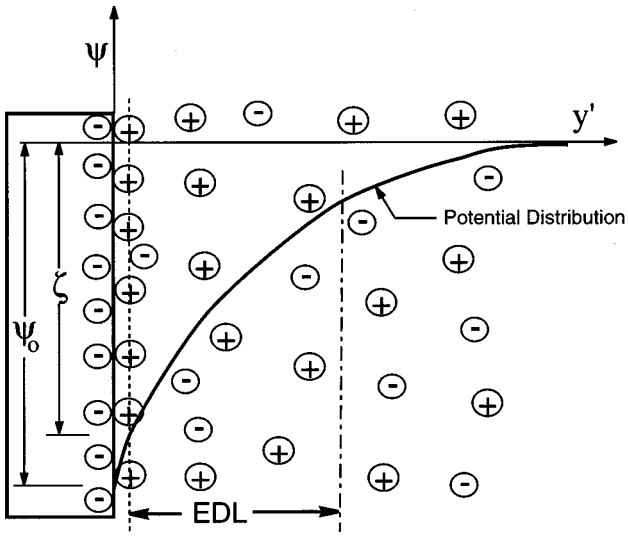

Fig. 1. Schematic diagram of EDL next to a negatively charged solid surface. Here ψ is the electric potential, ψ_o is the surface electric potential, ζ is the Zeta potential, and y' is the distance measured from the wall.

when a glass surface is immersed in water, it undergoes a chemical reaction in which fraction of the surface Si–OH bonds are changed to Si–O^-, which results in a net negative surface potential [1]. This influences the distribution of ions in the buffer solution, as shown in Fig. 1. Due to this surface electric potential, positive ions in the liquid get attracted to the wall. On the other hand, the negative ions get repelled from the wall, resulting in redistribution of the ions close to the wall, keeping the bulk of the liquid far away from the wall electrically neutral. The distance from the wall, where the electric potential energy is equal to the thermal energy is known as the Debye length (λ), and the region between the wall and λ is known as the electric double layer. The electric potential distribution within the fluid, due to the presence of the EDL is described by the Poisson–Boltzmann equation

$$\nabla^{*2}(\psi^*) = \frac{-4\pi h^2 \rho_e}{D\zeta} = \beta \sinh(\alpha\psi^*) \tag{1}$$

where ∇^* is the gradient operator nondimensionalized by a length scale h, $\psi^*(=\psi/\zeta)$ is the electroosmotic potential normalized with the Zeta potential ζ, ρ_e is the net electric charge density, D is the Dielectric constant and α is the ionic energy parameter given as

$$\alpha = ez\zeta/k_bT \tag{2}$$

where e is the electron charge, z is the valence, k_b is the Boltzmann constant and T is the temperature. The variable β relates the ionic energy parameter α and the characteristic length h to the Debye–Hückel parameter $\omega = (1/\lambda)$ as

$$\beta = \frac{(\omega h)^2}{\alpha}, \qquad \omega = \frac{1}{\lambda} = \sqrt{\frac{8\pi n_o e^2 z^2}{Dk_bT}}. \tag{3}$$

The Debye length (λ) is a function of the ion density n_o as given by equation (3). For aqueous solutions at 25 °C , the ion densities of 10^{-5}M and 10^{-3}M correspond to the Debye lengths of $\lambda \simeq 100$ nm, and $\lambda \simeq 10$ nm, respectively.

III. Governing Equations

The electroosmotic flow is generated when an external electric field ($\vec{E} = -\nabla\phi$) is applied in the presence of the EDL. This external electric field interacts with the electric double layer, and creates the electroosmotic body force on the fluid. The motion of ionized, incompressible fluid with electroosmotic body forces are governed by the incompressible Navier–Stokes equations:

$$\rho_f\left(\frac{\partial \vec{v}}{\partial t} + (\vec{v}.\nabla)\vec{v}\right) = -\nabla p + \mu\nabla^2\vec{v} + \rho_e\vec{E} \tag{4}$$

where p is the pressure, and $\vec{v}$ is a divergence free velocity field ($\nabla\cdot\vec{v} = 0$), ρ_f is the fluid density and μ is the dynamic viscosity. Here ρ_e is determined from the Poisson–Boltzmann equation (1), and the externally imposed electric potential (ϕ) is governed by

$$\nabla.(\sigma\nabla\phi) = 0 \tag{5}$$

where σ is the conductivity. The external electric field is subject to zero flux condition on the boundaries

$$\nabla\phi \cdot \vec{n} = 0. \tag{6}$$

The above equations are valid under the following assumptions and approximations: The fluid is Newtonian, and the fluid viscosity and permittivity are independent of the local or overall electric field strength, which is a valid approximation for dilute solutions. The ions are point charges, and the ionic-convection effects are negligible compared to the ionic-diffusion.

IV. Numerical Formulation and Validation

We used spectral element method for solution of the Poisson–Boltzmann and incompressible Navier–Stokes equations. The numerical algorithm employs *modal spectral expansions* in quadrilateral and unstructured triangular elements [15]. The unstructured mesh allows discretization of complex engineering geometries with great flexibility. However, it maintains high-order (spectral) accuracy for sufficiently smooth problems [15]. The Navier–Stokes algorithm is based on a third-order time accurate operator splitting scheme, and it is suitable for direct numerical simulation of flows in the Stokes, laminar and turbulent flow regimes. The details of this algorithm can be found in [15].

The Poisson–Boltzmann equation (1) is solved using a weak variational formulation based on the Galerkin projection. Since the Poisson–Boltzmann equation is nonlinear, we utilized a Newton iteration strategy for a variable coefficient Helmholtz equation. The exponential nonlinearity is treated in the following form:

$$[\nabla^{*2} - \alpha\beta\cosh(\alpha(\psi^*)^n)](\psi^*)^{n+1} = \beta\sinh(\alpha(\psi^*)^n) - \alpha\beta(\psi^*)^n\cosh(\alpha(\psi^*)^n)$$

where n shows the iteration number. The solution of a previous iteration is used for evaluation of the nonlinear forcing function, and the resulting system is solved until the residual is reduced beyond a certain level (typically, 10^{-13}).

The numerical solution of equation (1) is challenging due to the *exponential nonlinearity* associated with the hyperbolic-sine function. Especially for large values of α, the nonlinear forcing increases rapidly for any value of β, making the numerical solution challenging. For very large values of β with $\alpha = 1$, similar difficulties also exist. Accurate resolution of the problem requires high grid density within the EDL. A typical mesh structure for the $\alpha = 1$ and $\beta = 10\,000$ case is presented in Fig. 2 (bottom). The spectral element mesh has 22 elements across the channel width, spaced in biased fashion with minimum width of $0.001h$ very near the walls. Once the mesh topology is fixed, the modal expansion order N is increased to further resolve the problem. For rectangular elements shown in Fig. 2, $N = 2$ correspond to a quadratic solution in ψ^*, typically utilized by finite-element algorithms. In the spectral element method the basic mesh structure is fixed and successively higher values of modal expansion orders are utilized within each element to further resolve the problem.

In order to determine numerical accuracy of the algorithm, we used the analytical solution of one-dimensional Poisson–Boltzmann equation [4]:

$$\psi^*(\eta^*) = \frac{4}{\alpha}\tanh^{-1}\left[\tanh\left(\frac{\alpha}{4}\right)\exp\left(-\sqrt{\alpha\beta}\quad\eta^*\right)\right] \quad (7)$$

where, η^* is the normalized distance from the wall (i.e., $\eta^* = 1 - |y/h|$). In Fig. 2 (top) we present convergence results for $\alpha = 1$, $\beta = 10\,000$ by plotting the L_2 error norm as a function of the modal expansion order N. The results are obtained for the mesh topology shown on the bottom figure. The L_2 error norm is defined as

$$L_2 = \frac{\left[\int_\Omega R(\psi_N^*, \psi_A^*)^2\, d\Omega\right]^{1/2}}{\int_\Omega d\Omega}$$

where Ω shows the entire flow domain. The residual R is based on the difference between the numerical solution (ψ_N^*) and the analytical solution (ψ_A^*) given by equation (7). Convergence results presented in Fig. 2 show *exponential decay of the discretization error* with increased N, which is known as the spectral convergence. This high spatial resolution capacity enables us to accurately resolve thin EDLs with relatively less number of elements compared to the low-order algorithms.

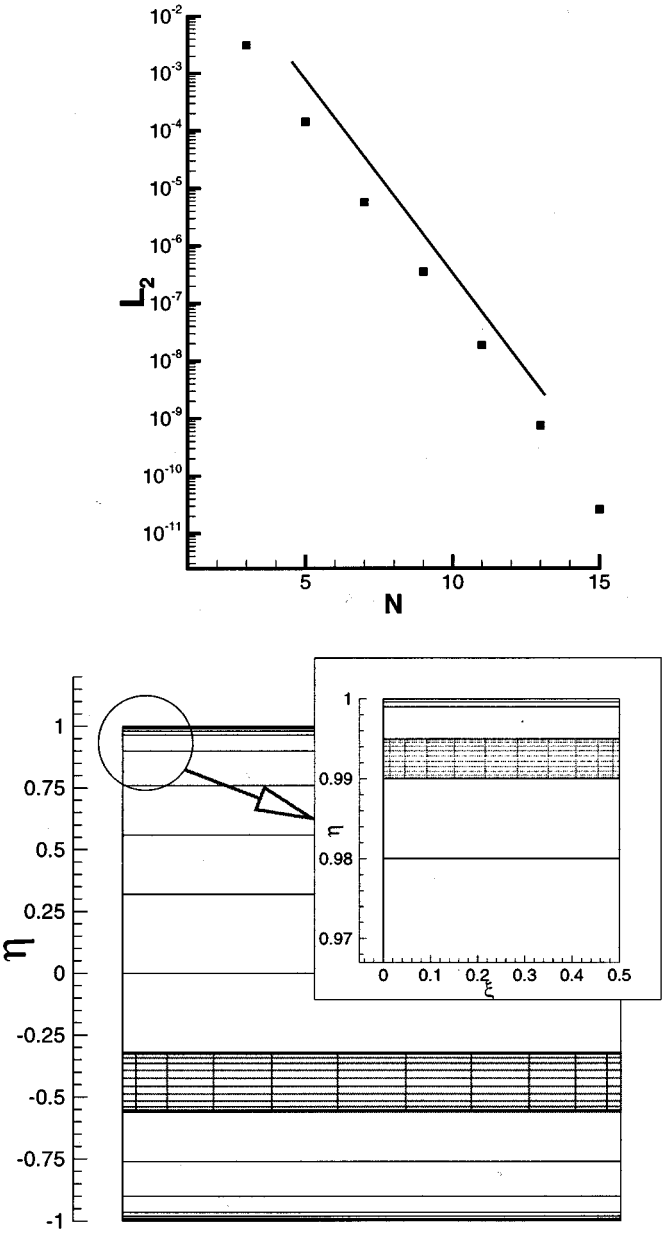

Fig. 2. Top: Spectral convergence in L_2 error norm as a function of the spectral expansion order N. Bottom: Sample grid used to resolve thin EDL region consists of 22 elements across the channel, and each element is discretized with Nth-order modal expansion per direction. The quadrature points for subelemental discretization for select elements are also shown. Simulations are performed for $\alpha = 1.0$ and $\beta = 10\,000$.

V. Electroosmotic Flow Control

Electroosmotic forces can be selectively applied for flow control in complex microgeometries by either utilization of local electric fields or by modification of surface Zeta potential (ζ). For example, the Zeta potential on the surface can be altered by contamination of the capillary walls, variations in the wall coating, or gradients in the buffer pH [7]. In this section, we will primarily study flow control in flow junctions using multiple electric fields by keeping the Zeta potential unaltered.

The simulation results presented in this section are performed for a dielectric material of $\zeta = -25.4$ mV and the half channel height of $h = 3$ μm, corresponding to $\alpha = 1$, $\beta = 10\,000$. The electroosmotic potential distribution (ψ^*) and the externally imposed electric field potential (ϕ) are obtained by solution of equations (1) and (5), respectively. The magnitude of the externally imposed electric field $||\vec{E}_o||$ corresponds to 950 V/cm, resulting in Helmholtz Smoluchowski velocity of $u_p = 1.6$ mm/s. We assumed that the buffer solution is water and the ion concentration density is $n_o = 0.1$ mM. The Reynolds number based on the average channel velocity and half channel height is $Re = 0.005$. These sets of simulation

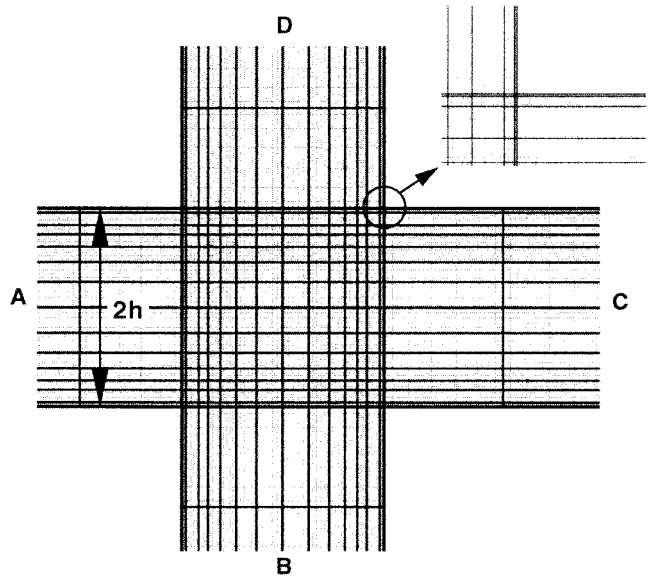

Fig. 3. A zoomed view of the spectral element discretization of the cross-flow junction geometry, with further magnification of the top right corner (inset). The black lines show spectral elements and gray lines correspond to the collocation points of a seventh-order spectral expansion per direction.

parameters are selected according to the data given by Hunter [16]. Here we must note that for $Re = 0.005$, we practically have Stokes flow with electroosmotic body forces, where the inertial forces are negligible and the velocity field is insensitive to the Reynolds number. Therefore, parametric studies as a function of the Reynolds number are not necessary in the Stokes flow limit.

A. Cross-Flow Junctions

The cross-flow junction of two micro-channels has many important applications in electrophoretic separation [8], [17] serial and parallel mixing [18] and species-transport control [19]. In this section, we applied two different electric fields in a cross-flow junction to demonstrate the flow behavior as a function of the applied electric field strength.

Computational Domain: A zoomed view of the cross flow junction, and its seventh-order spectral element discretization is shown in Fig. 3. The A, B, C and D branches are $2h$ wide, while the computational domain extends to $\pm 50h$ along each branch. Using this computational domain, we first solve the Poisson–Boltzmann equation (1) for the electroosmotic potential field (ψ^*). Since $\alpha = 1$ and $\beta = 10\,000$, the effective EDL thickness is about 4.5% of the half channel height [4]. Therefore, the electroosmotic potential field is essentially one-dimensional and the solution matches the analytical formula given by equation (7) in most of the domain, except near the corners.

1) Electric Field Analysis: In 1952, Overbeek proposed the irrotationality condition of internal electroosmotic flows for arbitrarily shaped geometries [20]. This is followed by the *ideal electroosmosis concept* of Cummings *et al.*, who showed similarity between the electric and the velocity fields under *specific* boundary conditions [21]. Recently, Santiago have shown that steady electroosmotic flow in the Stokes flow regime obey the irrotational bulk flow condition. However, for unsteady or high Reynolds number flows the bulk flow region may become rotational [22]. Based on these discussions detailed analysis of the electric field is essential for electroosmotic flows.

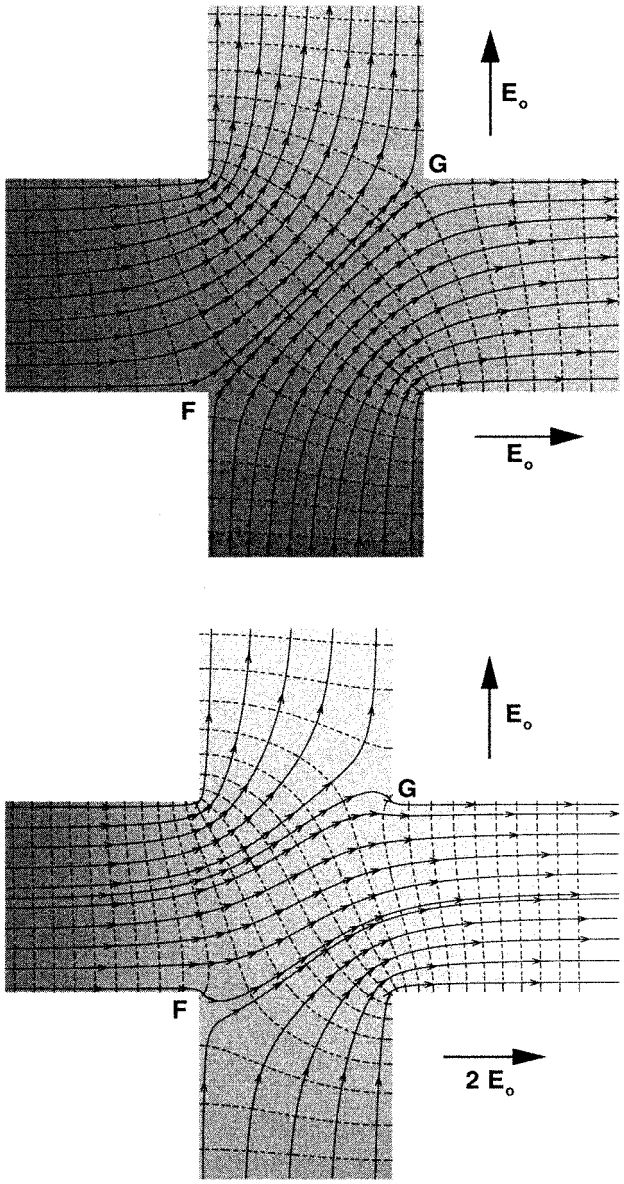

Fig. 4. Electric field lines (solid) and equipotential contours (dashed) in a cross-junction geometry, under various electric fields. Top: $E_{hor} = E_{ver} = E_o$. Bottom: $E_{hor} = 2E_{ver} = 2E_o$.

The externally imposed electric potential (ϕ) is determined by the electrostatic field equation (5) subject to the specified electric potential at the entrance/exit of the branches, and zero flux conditions on the walls. The electric field is constant and one-dimensional at the entry and exit regions of the channel. However, near the cross-junction the electric field is two-dimensional. In Fig. 4 we show the electric field lines obtained in the cross-junction under various horizontal and vertical electric field strengths. The figure shows equipotential contours with dash-lines and the electric field lines with solid lines. The electric field lines are orthogonal to the equipotential lines. For the equal horizontal and vertical electric field strength case, shown in the top Fig. 4, the electric field lines are symmetric with respect to the F–G plane. The electric field lines and equipotential

contours for the case of horizontal electric field being twice the vertical electric field ($E_{hor} = 2E_{ver}$) is shown in the bottom Fig. 4. Under bias electric field, the electric potential distribution is not symmetric any more. Interaction of two electric fields in the cross-junction creates dips in the electric field lines near points F and G. The curvature in the electric field lines near these corners are physical, and similar trends qualitatively exist in numerical results of Mitchell *et al.* obtained for a T-junction under bias electric field [12], and simulation results of Patankar and Hu, obtained in cross-flow junctions [9]. Here we also note that the electric potential is continuous around the corners, and the electric field lines are always orthogonal to the equipotential lines. Electric and electroosmotic potential fields, as well as their gradients were analyzed by Patankar and Hu in the vicinity of the corners [9]. Our simulation results agree with their analytical findings.

2) Flow Field Analysis: Once the electroosmotic potential and electric field are obtained, the electroosmotic body forces are calculated and utilized in the Navier–Stokes equations (4). The flow solver requires specification of the velocity profile at domain inlet(s) and imposes fully developed flow conditions at outflow(s). At the entrance of the channels we imposed "plug-like" velocity profile given in the following form [4]:

$$U(\eta^*) = 1 - \psi^*(\eta^*) = 1 - \frac{4}{\alpha}\tanh^{-1}\left[\tanh\left(\frac{\alpha}{4}\right)\exp(-\sqrt{\alpha\beta}\quad\eta^*)\right]. \quad (8)$$

For pure electroosmotic flows (i.e., without pressure gradients) the velocity is uniform in the bulk of the channel, and sharply varies within the EDL region in order to match the no-slip condition on the walls. This velocity distribution corresponds to a normalized volumetric flow rate of $\dot{Q}^* = 1.9803$, which can be obtained by

$$\dot{Q}^* = \frac{\dot{Q}}{u_p h} = 2\left(1 - \frac{\delta^*}{\sqrt{\alpha\beta}}\right) \quad (9)$$

where δ^* is the flowrate defect due to the EDL, defined in analogy to the *boundary layer displacement thickness in fluid mechanics* (Here for $\alpha = 1$, $\delta^* = 0.986\,35$) [4]. In equation (9), the term u_p is the Helmholtz–Smoluchowski electroosmotic velocity given by

$$u_p = -\frac{\zeta D\vec{E}_o}{4\pi\mu} \quad (10)$$

where $\vec{E}_o$ is the externally imposed electric field.

In Fig. 5 (top) we show the velocity vector field and the streamlines obtained for equal horizontal and vertical electric fields. The inlet channels A and B are subjected to equal flow rates. Uniform "plug like" velocity profiles are observed in all branches, with localized two-dimensional flow in the cross-junction. The velocity distribution within the EDL is also visible in the figure. Streamlines clearly show that flow entering from inlet A turns toward outlet channel D, and the flow entering from B leaves from outlet C. Comparison of the streamlines with electric field lines given in Fig. 4 (top) shows similarities between the velocity and the electric fields in the bulk flow region. Since the flow is driven by the electroosmotic forces, the pressure is uniform in the entire flow system. These findings closely agree with the theoretical results of [20]–[22].

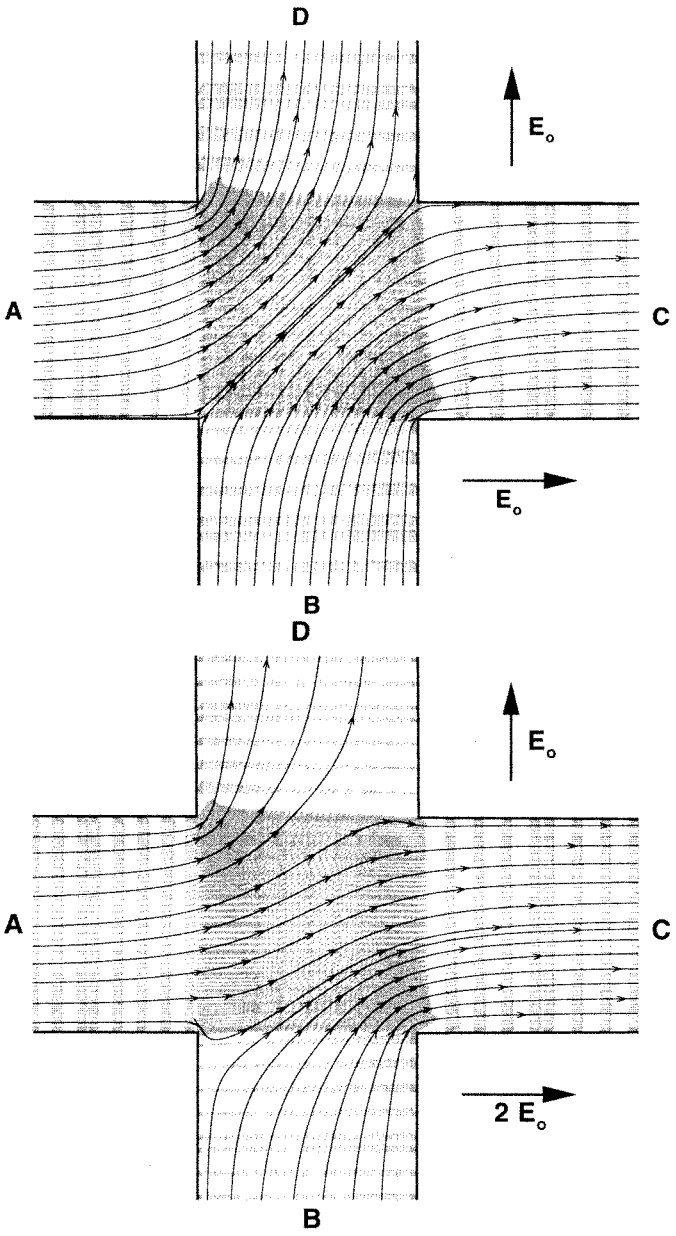

Fig. 5. The streamlines and velocity vectors for pure electroosmotic flow in a cross-flow junction (Only 25% of the vectors are shown for clarity of the figure). Top: $E_{hor} = E_{ver} = E_o$. Bottom: $E_{hor} = 2E_{ver} = 2E_o$.

In Fig. 5 (bottom) we show the velocity vectors and the streamlines obtained using a bias electric field with horizontal field being twice the vertical field ($E_{hor} = 2E_{ver}$). We specified the corresponding velocity distributions at the inlet of sections A and B, so that pure electroosmotic flow with twice the magnitude of branch B is maintained at inlet A. Similar to the equal electric field strength case shown in Fig. 5 (top), the flow in this case is driven solely by the electroosmotic body forces, hence the pressure field is uniform. A comparison of the streamlines with the electric field lines given in Fig. 4 (bottom) reveals similarities between the velocity and the electric fields in the bulk flow region, which agrees with the aforementioned theoretical findings.

In Fig. 5 (bottom) the velocity vectors at exit branch C show uniform plug profile of magnitude $2u_p$, similar to that of inlet branch A, while the exit branch D reaches a uniform plug profile of magnitude u_p, similar to that of inlet branch B. Under the bias electric field, the cross flow junction creates unique opportunities for flow control. If we examine the streamlines in the figure, it is clear that 50% of the fluid leaving from channel C is coming from inlet channel A. This is required by the bias electric field strength, and conservation of mass in the micro-fluidic system. Using this we conclude that it is possible to control the amount of fluid in exit channel C that is coming from inlets A and B, by controlling the ratio of the horizontal to vertical electric field (E_{hor}/E_{ver}). The ratio of the flowrates from inlets A and B at the exit channel C can be written in the following form:

$$\frac{\dot{Q}_{AC}}{\dot{Q}_{BC}} = \frac{E_{hor}}{E_{ver}} - 1 \tag{11}$$

where $\dot{Q}$ shows the flowrate, and the subscripts AC and BC show the contributions of flow from inlets A and B to the total flowrate in channel C, respectively. The above formula is subject to the following restriction:

$$\dot{Q}_A = \dot{Q}_C = \dot{Q}_{AC} + \dot{Q}_{BC} \tag{12}$$

due to the mass conservation requirements.

An interesting flow control scheme arises, if we are able to sustain a prescribed flowrate in the inlet channels A and B, by regulating the flowrate using micro-valves. For example, in the case of having equal volumetric flowrates at the entrance of channels A and B, under bias electric field strength of $E_{hor} = 2E_{ver}$ results in mixed electroosmotic/pressure driven flows in channels A, C and D. The velocity vectors and the corresponding streamlines are shown in Fig. 6. In addition to the electroosmotic body forces due to the biased electric field, local pressure forces cause more complicated flow fields than the bias pure electroosmotic flow case shown in Fig. 5 (bottom). The streamline patterns shown in Fig. 6 indicate flow control possibilities that are significantly different than the case presented in Fig. 5 and equation (11).

Streamwise velocity distribution in channels A–C and B–D are shown in Fig. 7. The velocity distributions are normalized by u_p, as $U = u/u_p$ and $V = v/u_p$. The streamwise velocity distribution in channels A, C and D show superposition of plug flow (due to the electroosmotic effects) and parabolic velocity profile due to the adverse pressure gradients. In the meantime, "plug flow" profile is observed in channel B.

The pressure distribution along the centerline for channels A–C and B–D are shown in Fig. 8. Here, the pressure values are normalized with $\mu u_p/h$, consistent with the Stokes flow nondimensionalization. We used equal channel lengths in all directions, and assume that the channel exits C and D are exposed to the atmospheric conditions (zero gauge pressure). Since we applied pure electroosmotic flow in channel B, the electrokinetic forces are balanced by the viscous forces, and no change in the pressure is observed in this region. The remaining three sections experience electroosmotic pumping due to higher electric field strength. Hence the entire cross junction system shown in Fig. 6 is self-sustained (under applied electric fields) and can be used in a "lab on a chip" system for precise delivery of various species from one channel to another.

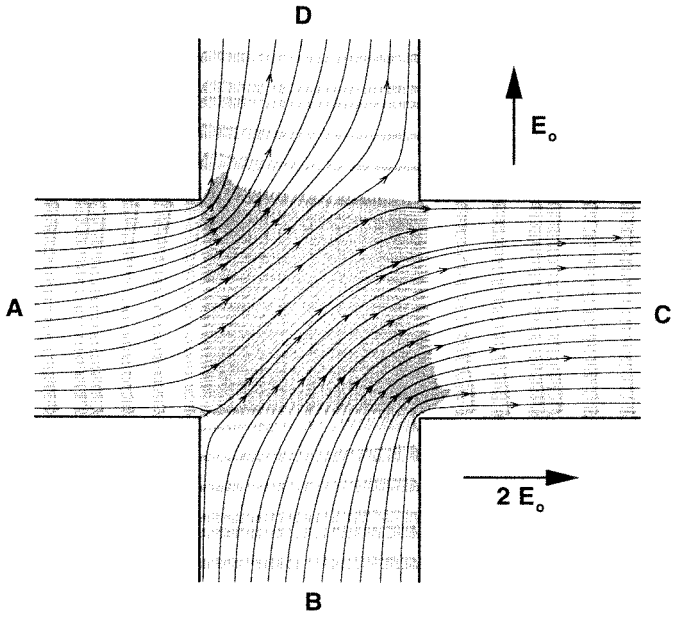

Fig. 6. The streamlines and velocity vectors for a mixed electroosmotic/pressure driven flow in a cross-flow junction, obtained by regulating the inlet flowrate in branches A and B ($\dot{Q}_A = \dot{Q}_B$). The electric field is such that $E_{hor} = 2E_{ver} = 2E_o$.

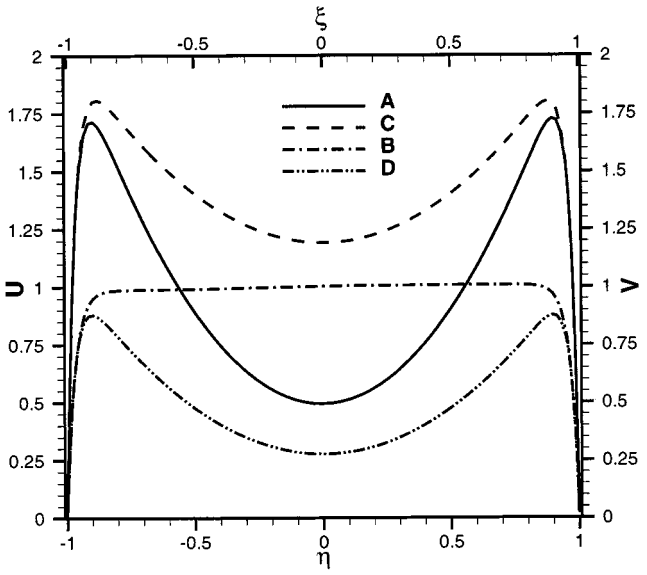

Fig. 7. Streamwise velocity distribution for mixed electroosmotic/pressure driven flow in cross-flow junction shown in Fig. 6. Channel B exhibits pure electroosmotic flow, but channels A, C, and D are subject to adverse pressure gradients due to the higher electric field strength than a locally sustainable pure electroosmotic flow.

Depending on the relative magnitude of E_{hor}/E_{ver}, we can control the amount of fluid pumped from channel A to channel C. We calculated the volumetric flowrate in channels C and D, and have shown that variation of the E_{hor}/E_{ver} ratio controls the flowrate in channels C and D *linearly*, as demonstrated in Fig. 9. This linear behavior is very important in flow/species control in micro-channel junctions. The results also show that

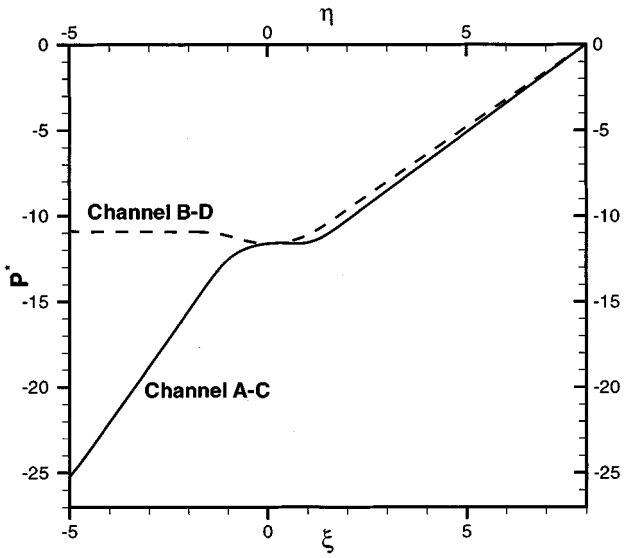

Fig. 8. Pressure variation along the centerline of channels A–C and B–D for the case of Fig. 6.

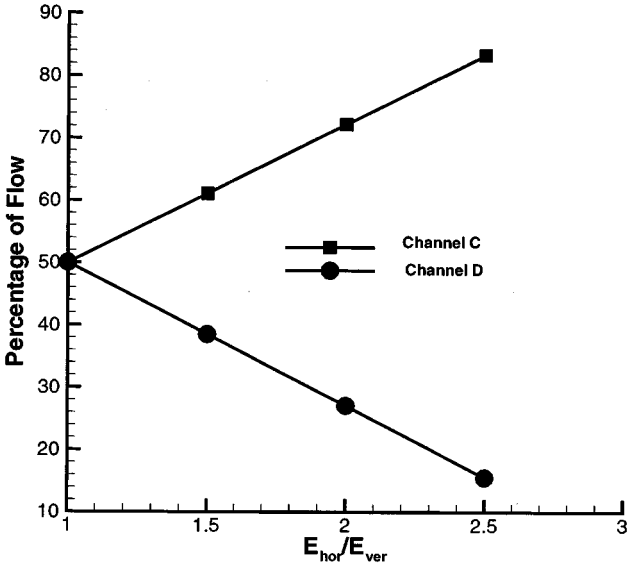

Fig. 9. Flow control through cross-flow junction in mixed electroosmotic/pressure driven flows. Variation of the channel exit flowrate as a function of the horizontal to the vertical electric field strength is shown. The flowrates at the inlet sections (A and B) are regulated here to result in equal flowrate at entry of both channels.

it is possible to block the flow in channel D completely, if $E_{hor}/E_{ver} = 2.8$ is applied.

B. Y-Split Channel

We applied electroosmotic forces to a Y-split channel to control the mass flowrate in its different branches (see Fig. 10). A fully developed flow corresponding to a plug-like velocity profile enters to the main branch A, and exits from the split branches B and C. Two different external electric fields along the A–B and A–C directions are applied in order to create the desired flow control effects.

Fig. 10 (top) shows the streamlines and the speed contours for the Y-split channel under equal electric field strength ($E_{AB} = E_{AC}$). Under this condition, the electroosmotically

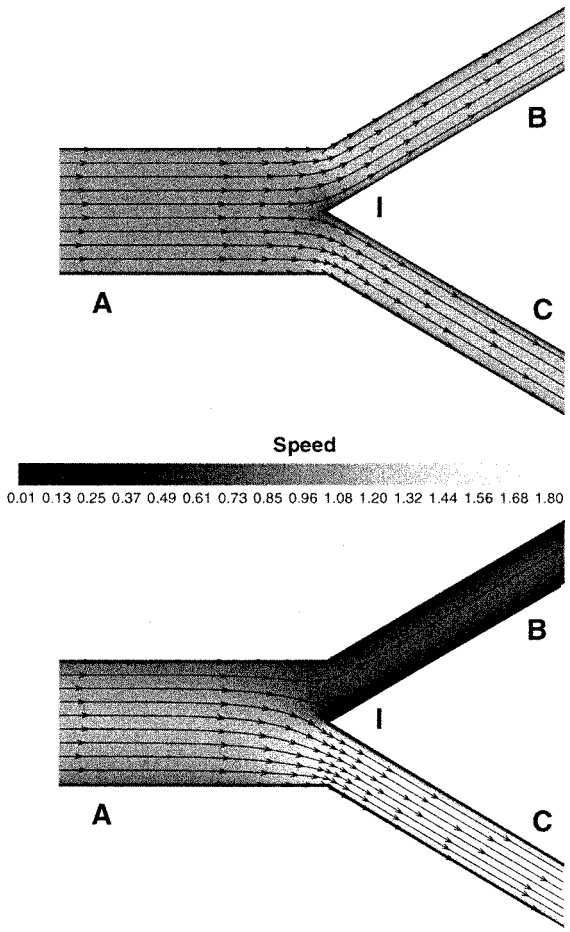

Fig. 10. Streamlines and speed contours for electroosmotic flow in a Y-split channel. The numerical simulations are performed for $\alpha = 1$ and $\beta = 10\,000$ at $Re = 0.005$. Top: $E_{AB} = E_{AC}$. Bottom: $E_{AC} = 3E_{AB}$.

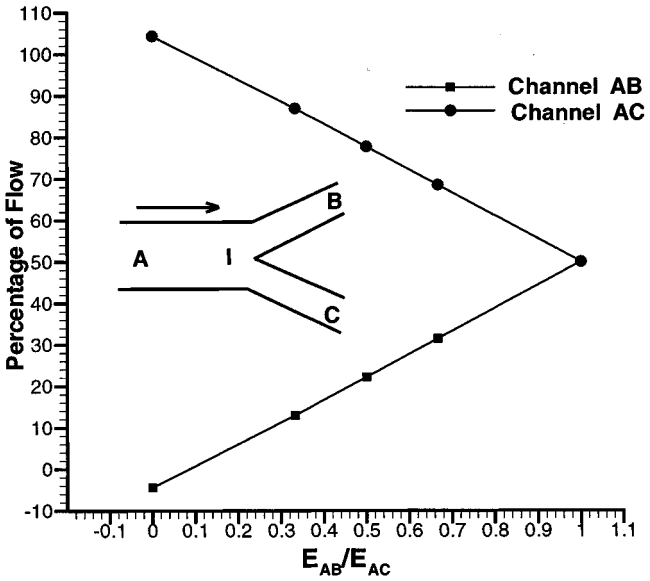

Fig. 11. Flow rate variation in the branches of the Y-split junction as a function of the E_{AB}/E_{AC} ratio.

driven flow is divided uniformly into the two branches (B and C). The flow control along the Y-split can be obtained by changing the magnitude of the E_{AB}/E_{AC}. One representative

case is $E_{AC}/E_{AB} = 3$, where substantial amount of flow is deflected toward branch-C due to the higher electric field strength along the A–C direction. The speed contours and the streamlines for this case are shown in the bottom figure.

Fig. 11 shows the flowrate in the B- and C-branches as a function of the E_{AB}/E_{AC} ratio. The flowrate in each branch can be altered by changing the E_{AB}/E_{AC} ratio. For $E_{AB}/E_{AC} = 0.0433$, flow in branch-B can be completely blocked. At smaller values of the E_{AB}/E_{AC} ratio, the flow suction from branch-B is observed. Here we must emphasize that the *flowrate variation as a function of the electric field ratio is linear*. Hence, this technique can also be used in flow control for various microfluidic applications.

VI. Conclusion

We presented numerical simulation results for pure electroosmotic and mixed electroosmotic/pressure driven flows in various microchannel geometries. In the cross-flow junction, we analyzed pure electroosmotic flows with equal and bias electric fields. We have shown that the velocity field in the bulk flow region (outside the EDL) follows the electric field lines. We also studied a *regulated* flowrate system with equal inlet flowrates and have identified mixed pressure/electroosmotic flows under bias electric fields.

We have shown that the effect of the electroosmotic body forces on flowrate is *linear* in the Stokes flow regime. This linear response can be utilized to design electroosmotically actuated micropump/valve systems and various flow switches. For example, the cross-flow junction can be used for dispensing *precise amount of fluid* from one channel to another. The Y-split junction can be utilized as a flowrate control device, where a fluctuating (quasi-steady) electric field can be utilized to maintain a time-periodic flow in the downstream region. Local application of electric fields in the cross-flow and Y-junctions can create *nonmechanical flow switching mechanisms* between various branches of micro-fluidic systems.

Finally, due to the difficulties involved in experimenting in micro-scales, it is desirable to develop *reliable numerical models*, which can *accurately describe* fluid flow in *complex micro-geometries*. Our numerical methodology has the flexibility of utilizing mixed unstructured/structured grid topology for discretization of complex geometries. At the same time, the algorithm delivers high-order accuracy, which enables accurate resolution of thin EDL regions. Such numerical algorithms can be used for design of *optimized* microfluidic systems, *prior* to hardware fabrication and experimental verification.

Acknowledgment

The computational facilities provided by the Dell STAR Program are appreciated. The authors would like thank Dr. S. Devasenathipathy for his careful review of this article.

References

[1] R. F. Probstein, *Physiochemical Hydrodynamics*. New York: Wiley, 1994.

[2] D. Burgreen and F. R. Nakache, "Electrokinetic flow in ultrafine capillary silts," *J. Phys. Chem.*, vol. 68, no. 5, pp. 1084–1091, 1964.

[3] H. Ohshima and T. Kondo, "Electrokinetic flow between two parallel plates with surface charge layers: Electroosmosis and streaming potential," *J. Colloids Interface Sci.*, vol. 135, no. 2, pp. 443–448, 1990.

[4] P. Dutta and A. Beskok, "Analytic solution of combined electroosmotic/pressure driven flows in two-dimensional straight channels: Finite Debye layer effects," *Anal. Chem.*, vol. 73, no. 9, pp. 1979–1986, 2001.

[5] C. L. Rice and R. Whitehead, "Electro kinetic flow in a narrow cylindrical capillary," *J. Phys. Chem.*, vol. 69, pp. 4017–4023, 1965.

[6] P. H. Paul, M. G. Graguilo, and D. J. Rakestraw, "Imaging of pressure and electrokinetically driven flows through open capillaries," *Anal. Chem.*, vol. 70, pp. 2459–2467, 1998.

[7] A. E. Herr, J. I. Molho, J. G. Santiago, M. G. Mungal, T. W. Kenny, and M. G. Garguilo, "Electroosmotic capillary flow with non uniform zeta potential," *Anal. Chem.*, vol. 72, pp. 1053–1057, 2000.

[8] N. A. Polson and M. A. Hayes, "Electroosmotic flow control of fluids on a capillary electrophoresis microdevice using an applied external voltage," *Anal. Chem.*, vol. 72, no. 10, pp. 1088–1092, 2000.

[9] N. A. Patankar and H. H. Hu, "Numerical simulation of electroosmotic flow," *Anal. Chem.*, vol. 70, pp. 1870–1881, 1998.

[10] S. V. Ermakov, S. C. Jacobson, and J. M. Ramsey, "Computer simulation of electrokinetic transport in micro fabricated channel structures," *Anal. Chem.*, vol. 70, pp. 4494–4504, 1998.

[11] F. Bianchi, R. Ferrigno, and H. H. Girault, "Finite element simulation of an electroosmotic-driven flow division at a t-junction of microscale dimension," *Anal. Chem.*, vol. 72, pp. 1987–1993, 2000.

[12] M. J. Mitchell, R. Qiao, and N. R. Aluru, "Meshless analysis of steady-state electro-osmotic transport," *J. Microelectromech. Syst.*, vol. 9, no. 4, pp. 435–449, 2000.

[13] C. Yang and D. Li, "Analysis of electrokinetic effects on the liquid flow in rectangular microchannels," *J. Colloids Surfaces*, vol. 143, pp. 339–353, 1998.

[14] G. M. Mala, D. Li, and J. D. Dale, "Heat transfer and fluid flow in microchannels," *Int. J. Heat Mass Trans.*, vol. 40, pp. 3079–3088, 1997.

[15] G. E. Karniadakis and S. J. Sherwin, *Spectral/HP Element Methods for CFD*. Oxford, U.K.: Oxford University Press, 1999.

[16] R. J. Hunter, *Zeta Potential in Colloid Science: Principles and Applications*. New York: Academic, 1981.

[17] C. T. Culbertson, R. S. Ramsey, and J. M. Ramsey, "Electroosmotically induced hydraulic pumping on microchips: Differential ion transport," *Anal. Chem.*, vol. 72, no. 10, pp. 2285–2291, 2000.

[18] S. C. Jacobson, T. E. McKnight, and J. M. Ramsey, "Microfluidic devices for electrokinetically driven parallel and serial mixing," *Anal. Chem.*, vol. 71, pp. 4455–4459, 1999.

[19] E. B. Cummings, S. K. Griffiths, and R. H. Nilson, "Irrotationality of uniform electroosmosis," in *Proc. SPIE Microfluidic Devices and Systems II*, Santa Clara, CA, Sept. 20–21, 1999.

[20] J. T. G. Overbeek, *Colloid Science*, H. R. Kruyt, Ed. Amsterdam: Elsevier, 1952, vol. 1.

[21] E. B. Cummings, S. K. Griffiths, R. H. Nilson, and P. H. Paul, "Conditions for similitude between the fluid velocity and electric field in electroosmotic flow," *Anal. Chem.*, vol. 72, pp. 2526–2532, 2000.

[22] J. Santiago, "Electroosmotic flows in microchannels with finite inertial and pressure forces," *Anal. Chem.*, vol. 73, pp. 2353–2365, 2001.

Prashanta Dutta received the B.Sc. and M.Sc. engineering degrees in mechanical engineering from Bangladesh University of Engineering and Technology (BUET), Dhaka, Bangladesh, in 1993 and 1995, respectively. He received the M.S.M.E. degree from the University of South Carolina, Columbia, SC, in 1997 and the Ph.D. degree from Texas A&M University, College Station, TX, in 2001.

In fall 2001, he joined the School of Mechanical and Materials Engineering of Washington State University, Pullman as an Assistant Professor. His current research focus is on nano-scale transport modeling, microscale flow visualization, and microheat engines.

Ali Beskok received the B.S. degree in mechanical engineering from Middle East Technical University, Ankara, Turkey, in 1988. He received the M.S. degree in mechanical engineering from Indiana University, Purdue University in Indianapolis in 1991. He received the M.S. and Ph.D. degrees in mechanical and aerospace engineering from Princeton University, Princeton, NJ, in 1994 and 1996, respectively.

From 1994 to 1996, he was a Visiting Research Scholar at Brown University Center for Fluid Mechanics, Providence, RI, and from 1996 to 1998, a Postdoctoral Research Associate at Massachusetts Institute of Technology, Research Laboratory of Electronics. In 1998, he joined Texas A&M University Mechanical Engineering Department, College Station, where he is presently an Assistant Professor. His current research focuses are on micro- and nanoscale thermal/fluidic transport, rarefied gas dynamics, fluid/structure interaction, and numerical simulation techniques such as the direct simulation Monte Carlo and spectral element methods.

Timothy C. Warburton received the B.A. degree in mathematics from the University of Oxford, Oxford, U.K., in 1993. He received the M.Sc. and Ph.D. degrees in applied mathematics from Brown University, Providence, RI, in 1994 and 1999, respectively.

From 1998 to 1999, he was a Research Officer in the Oxford University Computing Laboratory and from 1999 to 2001, he was a Visiting Research Associate in the Division of Applied Mathematics, Brown University. In fall 2001, he joined the University of New Mexico as an Assistant Professor in the Department of Mathematics and Statistics. Dr. Warburton's research is focused on creating robust, flexible and efficient high-order finite element algorithms for numerical solution of partial differential equations of fluid mechanics, plasma physics, and electromagnetics.